Chemical Science

ROYAL SOCIETY OF CHEMISTRY

EDGE ARTICLE

View Article Online
View Journal | View Issue

Cite this: *Chem. Sci.*, 2025, **16**, 14724

All publication charges for this article have been paid for by the Royal Society of Chemistry

Received 26th April 2025
Accepted 9th July 2025

DOI: 10.1039/d5sc03041b

rsc.li/chemical-science

Synergistic intercalation–conversion reaction mechanism in Prussian blue analogue materials toward enhanced Na-storage†

Na Liu,‡ Xiaohan Wang,‡ Jing Liu, Ningbo Liu and Liubin Wang *

Sodium-ion batteries (SIBs) have emerged as promising candidates for large-scale energy storage systems owing to the abundant and low-cost sodium resources. Among various cathode materials, Prussian blue analogues (PBAs) show great promise due to their three-dimensional open framework and easy synthesis process. However, critical challenges including limited electron transfer, blocked electronic pathways between particles, excessive lattice water content, and structural instability during cycling significantly compromise their electrochemical performance. Herein, we have developed a lead hexacyanoferrate/carbon nanotube composite (PbHCF/CNTs) through rational interface design to improve the electrochemical performance. The PbHCF/CNTs electrode exhibits a four-electron transfer capacity based on the redox reaction of $Pb^{0/2+}$ through a reversible intercalation–conversion mechanism. This innovative configuration delivers a high initial reversible capacity of 161.8 mA h g^{-1} at 20 mA g^{-1} and good cycling stability with 95.8 mA h g^{-1} retained after 250 cycles at 100 mA g^{-1} (64% capacity retention), along with enhanced structural reversibility confirmed by *operando* XRD analysis. This innovative approach provides a new design concept for high-capacity Prussian blue analogue cathode materials in the realm of high-performance SIBs and beyond.

Introduction

The increasing global energy demands have heightened the focus on developing cost-effective and high-performance rechargeable battery systems.[1–3] Sodium-ion batteries (SIBs) are emerging as particularly promising candidates for grid-scale energy storage applications, owing to sodium's natural abundance and significantly lower material costs compared to lithium counterparts.[4–7] Substantial research efforts have been directed toward developing advanced cathode materials through structural engineering and interface optimization strategies, with particular emphasis on layered transition metal oxides, polyanionic compounds, organic compounds, and Prussian blue analogues (PBAs).[8–14] Among these, PBAs demonstrate exceptional potential due to their unique open framework structure, facile synthesis process, and tunable redox chemistry.[15–17] However, the limited electron transfer, high crystalline water and vacancy content in PBAs result in low capacity and poor cycling stability, impeding their widespread application in SIBs.[18–20] Therefore, it is crucial to develop high-capacity PBA cathode materials with long lifespan for the next generation of SIBs.

The typical chemical formula of PBAs is $A_{2-x}M[Fe(CN)_6]_{1-y}\square_y\cdot nH_2O$, (A = Na, K, M = transition metal ions such as Fe, Co, Ni, Cu, Zn, *etc.*, $\square$ = $Fe(CN)_6$ vacancies usually occupied by H_2O, $0 < x < 2$, $0 < y < 1$).[21–23] Based on the structure of the two redox-active sites, M^{2+}/M^{3+} and Fe^{2+}/Fe^{3+}, the PBAs predominantly involve single-electron transfer (M = Cu, Co, Zn, *etc.*) and double-electron transfer (M = Mn, Fe, Cr, *etc.*), with respective theoretical capacities of approximately 85 mA h g^{-1} and 170 mA h g^{-1}.[24–28] Recent studies have shown that $Na_{1.72}MnFe(CN)_6$ exhibits a specific capacity of 134 mA h g^{-1} at a current density of 0.05C as a cathode for SIBs, demonstrating good rate performance.[29] Nevertheless, challenges such as electron-connecting channel between blockages poor electron conductivity, structural instability, electrolyte side reactions, and low capacities have impeded the widespread utilization of PBAs in SIBs.[30,31] To overcome these obstacles, extensive research has focused on the structural optimization of PBAs, carbon composites, and the enhancement of metal ions bound to N atoms within the –C≡N– group, aiming to enhance Na-storage capacity and electrochemical performance.[32–36] However, these approaches remain constrained by the intrinsic two-electron transfer limitation of conventional transition metal redox centers.

College of Chemistry and Materials Science, Key Laboratory of Analytical Science and Technology of Hebei Province, Hebei Research Center of the Basic Discipline of Synthetic Chemistry, Hebei University, Baoding, Hebei 071002, China. E-mail: lbwang@hbu.edu.cn

† Electronic supplementary information (ESI) available. See DOI: https://doi.org/10.1039/d5sc03041b

‡ The authors contribute equally to this work.

Herein, we report a breakthrough in multi-electron redox chemistry enabled by a lead-based hexacyanoferrate ($Pb_2Fe(CN)_6$, PbHCF) synthesized *via* a scalable co-precipitation approach. The material features a three-dimensional open framework with exceptional reversible Na-storage capabilities. To further enhance electrochemical performance, a composite cathode material (PbHCF/CNTs) was engineered by integrating the PbHCF framework with carbon nanotubes (CNTs), thereby constructing an uninterrupted conductive network. The unique hierarchical structure of this Pb-based ferrocyanide not only facilitates efficient Na^+ migration and diffusion but also effectively accommodates substantial volume variations during cycling. Electrochemical characterization revealed that the PbHCF/CNTs composite achieves an enhanced sodium-storage capacity *via* a four-electron transfer mechanism centered on the Pb^{2+}/Pb^0 redox couple. The composite demonstrates superior specific capacity retention (95.8 mA h g^{-1} after 250 cycles at 100 mA g^{-1}, corresponding to 85% capacity retention), cycling stability, and rate capability compared to pristine PbHCF. Mechanistic investigations employing multimodal characterization techniques (*operando* XRD, *in situ* FTIR, and *ex situ* XPS) confirmed that the *in situ* generation of metallic lead (Pb^0) during discharge significantly improves electron transport kinetics while promoting Na^+ diffusion. Furthermore, a full-cell configuration using hard carbon as the anode (HC||PbHCF/CNTs) demonstrated promising practical performance, highlighting its potential for energy storage applications. This innovative multi-electron redox strategy with synergistic intercalation–conversion reaction mechanism provides a generalizable design paradigm that could be extended to other ferrocyanide-based coordination materials for advanced electrochemical energy storage systems.

Results and discussion

PbHCF nanoparticles with a three-dimensional layer network structure were synthesized using a facile co-precipitation method. To address the inherent conductivity limitations, we strategically integrated carbon nanotubes (CNTs) during the nucleation stage of PbHCF, forming PbHCF/CNTs composites. This strategic integration enabled the establishment of a continuous conductive pathway throughout the hybrid matrix while maintaining structural integrity. The crystallographic properties of both pristine PbHCF and PbHCF/CNTs composites were systematically investigated using X-ray diffraction (XRD). Rietveld refinement analysis of the PbHCF/CNTs XRD pattern, as shown in Fig. 1a, confirmed the preservation of the orthorhombic phase with *Cmcm* space group (PDF#48-0225), demonstrating high crystallinity.[37] The refined unit cell parameters for PbHCF are shown in Table S1,† specifically, $a = 7.163998$ Å, $b = 7.163998$ Å, $c = 5.431422$ Å, $\alpha = \gamma = 90°$, $\beta = 120°$, and $V = 241.41$ Å^3. Characteristic diffraction peaks at 14.3° (100), 16.3° (001), 21.7° (101), 24.9° (110), 29.9° (111), and 33.3° (201) remained consistent between the PbHCF/CNTs composite and pristine PbHCF (Fig. S1†), indicating that CNT incorporation did not compromise the intrinsic three-dimensional network architecture.[38,39] Fig. 1b illustrates the fundamental building blocks of the PbHCF framework, comprising PbN_6 polyhedra and FeC_6 octahedra interconnected through cyanide (C≡N) bridges. High-resolution transmission electron microscopy (HRTEM) analysis (Fig. 1c) revealed interplanar spacings of 0.298 nm and 0.615 nm, corresponding to the (111) and (100) crystallographic planes, respectively. The measured interfacial angle of 44.2° between these planes aligns well with theoretical values for the orthorhombic system in the XRD patterns of PbHCF/CNTs (Fig. 1a). To elucidate the enhanced conductivity mechanism, we performed first-principles calculations on the electronic structures of both materials. As shown in Fig. 1d, pristine PbHCF exhibits semiconducting behavior with a direct bandgap of 2.97 eV from the density of state (DOS) calculations. Remarkably, CNTs integration substantially reduced this bandgap to 0.93 eV (Fig. S2†), suggesting improved charge carrier mobility. This theoretical prediction was experimentally validated by two-terminal device measurements (Fig. S3†), revealing a sixfold enhancement in conductivity from 0.23 S m^{-1} for PbHCF to 1.41 S m^{-1} for the PbHCF/CNTs composite. The synergistic combination of CNT-mediated electron transport and preserved crystalline framework accounts for this significant conductivity improvement.

The spectral characteristics of PbHCF/CNTs were analyzed using Raman and Fourier-transform infrared (FTIR) techniques. Raman spectra in Fig. 2a displayed characteristic vibrations at 186 cm^{-1} (ν (Fe–C)), 2159 cm^{-1} (C≡N stretching), and 2050 cm^{-1} (Fe–CN–Fe), with a distinct Pb–N coordination peak at 400 cm^{-1}. The emergence of D-band (1348 cm^{-1}) and G-band (1588 cm^{-1}) signatures confirmed CNTs incorporation and interfacial interactions with the PbHCF matrix.[39] FTIR analysis (Fig. 2b) further validated structural preservation, showing a strong absorption peak at 2028 cm^{-1} in PbHCF/CNTs associated with C≡N, and characteristic absorption peaks at 594 cm^{-1} and 425 cm^{-1} attributed to Fe–C and Pb–N bonds, respectively.[40] The vibrational modes of PbHCF/CNTs were found to be identical to those of PbHCF, indicating that the incorporation of CNTs did not alter the structural composition of PbHCF. Pristine PbHCF exhibited distinct O–H stretching vibrations at 1618 cm^{-1} and 3620 cm^{-1}, indicating the presence of crystal water in the metal–organic framework. Remarkably, these hydration signatures disappeared in the PbHCF/CNTs composite, suggesting that CNT incorporation effectively suppresses lattice vacancy formation and enhances structural stability. This observation was also corroborated by thermogravimetric analysis (TGA). As shown in the TGA (Fig. S4†), PbHCF has almost no weight loss before 100 °C and a weight loss of 3.7% before 200 °C, which may be related to the loss of intercalated water. The weight drops significantly from 200 °C to 354 °C, which is due to the loss of coordination water. Notably, the total water content (8.0%) in PbHCF was substantially lower than typical PBAs, and complete hydration elimination occurred upon CNT integration. The calculated CNT mass loading in the PbHCF/CNTs reached 12.8%, consistent with the improved structural integrity observed in XRD patterns.

The chemical composition and surface electronic states of PbHCF/CNTs were further investigated using X-ray

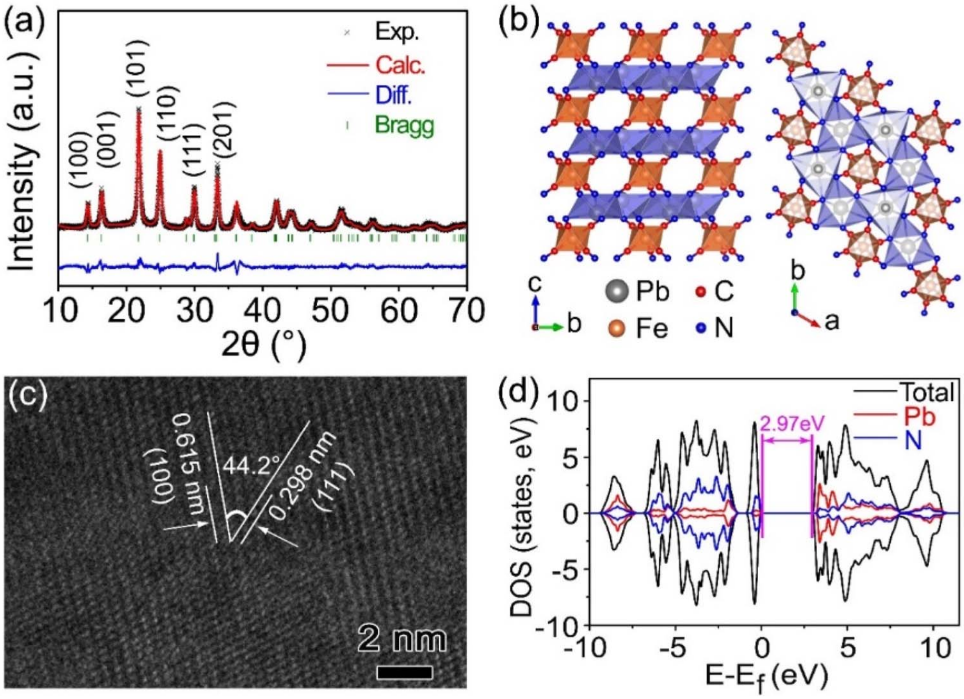

Fig. 1 (a) Structural refinement of XRD patterns of PbHCF/CNTs; (b) crystal structure of PbHCF consisting of layer structure with PbN_6 (blue) and FeC_6 (orange) polyhedra; (c) HRTEM image of PbHCF/CNTs; and (d) DOS of PbHCF.

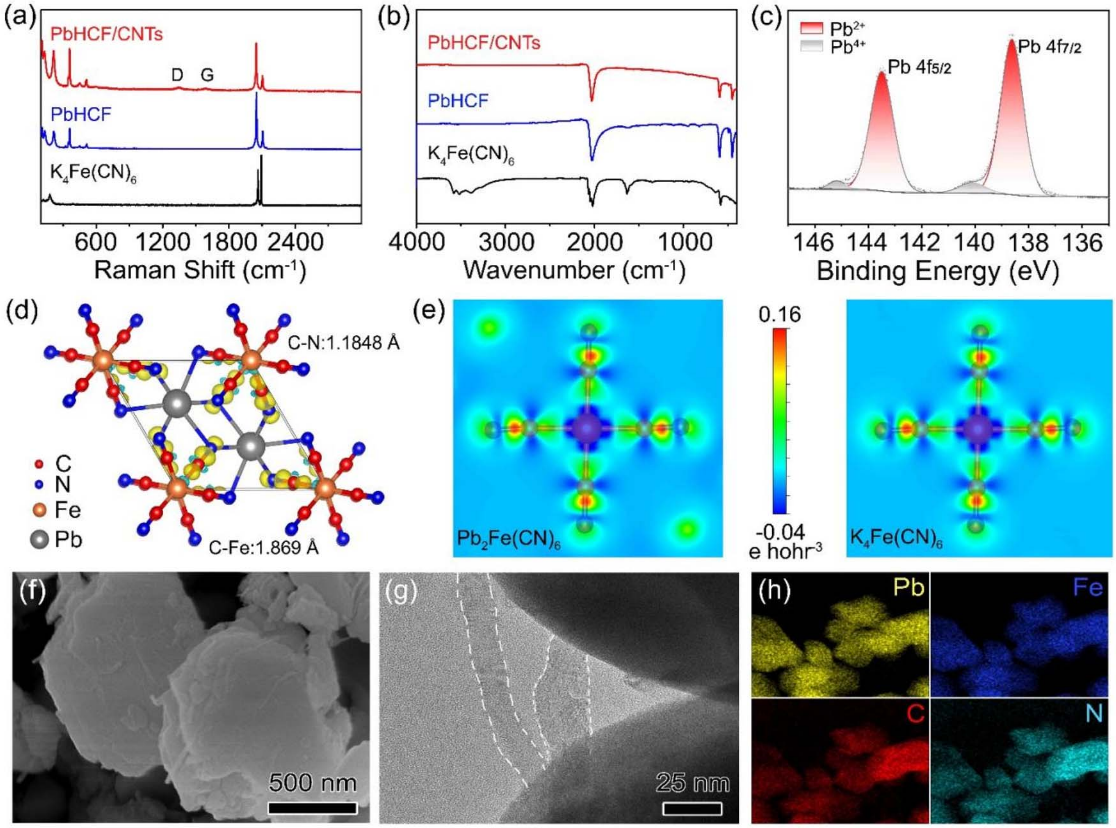

Fig. 2 (a) Raman and (b) FTIR spectra of KHCF, PbHCF, and PbHCF/CNTs; (c) Pb 4f XPS spectra of the PbHCF/CNTs; (d) diagram of the coordination structure and bond length of PbHCF; (e) the 2D electrons density mapping of PbHCF and KHCF; (f) SEM, (g) HRTEM images and (h) elemental mappings of PbHCF/CNTs.

photoelectron spectroscopy (XPS). The survey spectrum in Fig. S5† confirmed the presence of Pb, Fe, C and N elements. We can find four different peaks in the high-resolution XPS spectrum of Pb 4f in Fig. 2c. It is clear that the two main peaks at 138.65 eV and 143.5 eV are attributed to Pb^{II} $4f_{7/2}$ and Pb^{II} $4f_{5/2}$, respectively. In addition, there is a weak double peak at 140.1 eV and 145.2 eV for Pb^{IV} $4f_{7/2}$ and Pb^{IV} $4f_{5/2}$, suggesting surface oxidation during synthesis. Fe 2p XPS spectra with diffraction peaks at 708.75 eV and 721.55 eV was also observed in Fig. S5b,† which can be attributed to Fe $2p_{1/2}$ and Fe $2p_{3/2}$, respectively. Analysis of the C ls peaks (Fig. S5c†) at 284.45 eV, 285.25 eV, 286.15 eV, and 290.45 eV revealed the presence of C–C, C–N, C≡N, and C–F bonds in the PbHCF/CNTs samples, confirming the presence of CNTs. Furthermore, the XPS N 1s spectra (Fig. S5d†) showed peaks corresponding to C–N at 397.85 eV and C≡N at 400.1 eV, indicating the presence of cyano ligand N in the samples.[41] As shown in Fig. 2d, upon coordination with ferrocyanide, PbHCF exhibits shortened C–N (1.1848 Å) and Fe–C (1.8690 Å) bond lengths compared to that of the pristine KHCF (Fig. S6†), thereby enhancing the structural stability. Density functional theory (DFT) calculations (Fig. 2e) revealed enhanced electron delocalization through Pb-mediated charge redistribution, effectively lowering activation energy for redox processes. This unique PbHCF structure facilitates the exchange of effective electrons, leading to highly reversible redox reactions and ultimately contributing to enhanced electrochemical performance.

The morphology and structure of PbHCF/CNTs and PbHCF samples were studied by Scanning electron microscopy (SEM) and TEM. The PbHCF/CNTs have a size of about 700 nm (Fig. 2f and S7†), which is evenly distributed and larger than PbHCF (~500 nm, Fig. S8†). This was due to the incorporation of CNTs, which resulted in improved crystallinity and size uniformity, consistent with XRD results (Fig. 1a and S1†). Further examination of Fig. 2g and S9† showed that PbHCF/CNTs were monodispersed in the CNTs network, forming a chain-like architecture through CNT-guided heteroepitaxial growth. This unique microstructure is caused by nucleation and growth of PbHCF heterosites in carbon nanotubes during synthesis. The strong adhesion of PbHCF to CNTs promoted the electronic contact between PbHCF and CNTs and established a continuous conductive network. Elemental mapping (Fig. 2h) confirmed homogeneous spatial distribution of Pb, Fe, C, and N throughout the composite, validating the successful construction of three-dimensional conductive frameworks. The energy dispersive X-ray spectroscopy data presented in Fig. S10† and the results from inductive coupled plasma-optical emission spectrometry (ICP-OES) in Table S2† confirm the alignment of the chemical composition with the structural formula. This hierarchical architecture of PbHCF/CNTs accounts for the enhanced charge transfer kinetics observed in electrochemical testing.

The electrochemical properties of PbHCF/CNTs and pristine PbHCF electrodes were systematically investigated within the voltage range of 1.1–3.8 V through cyclic voltammetry (CV), galvanostatic charge–discharge (GCD), and electrochemical impedance spectroscopy (EIS). As illustrated in Fig. 3, the PbHCF/CNTs composite demonstrates significantly enhanced electrochemical performance compared to PbHCF, validating

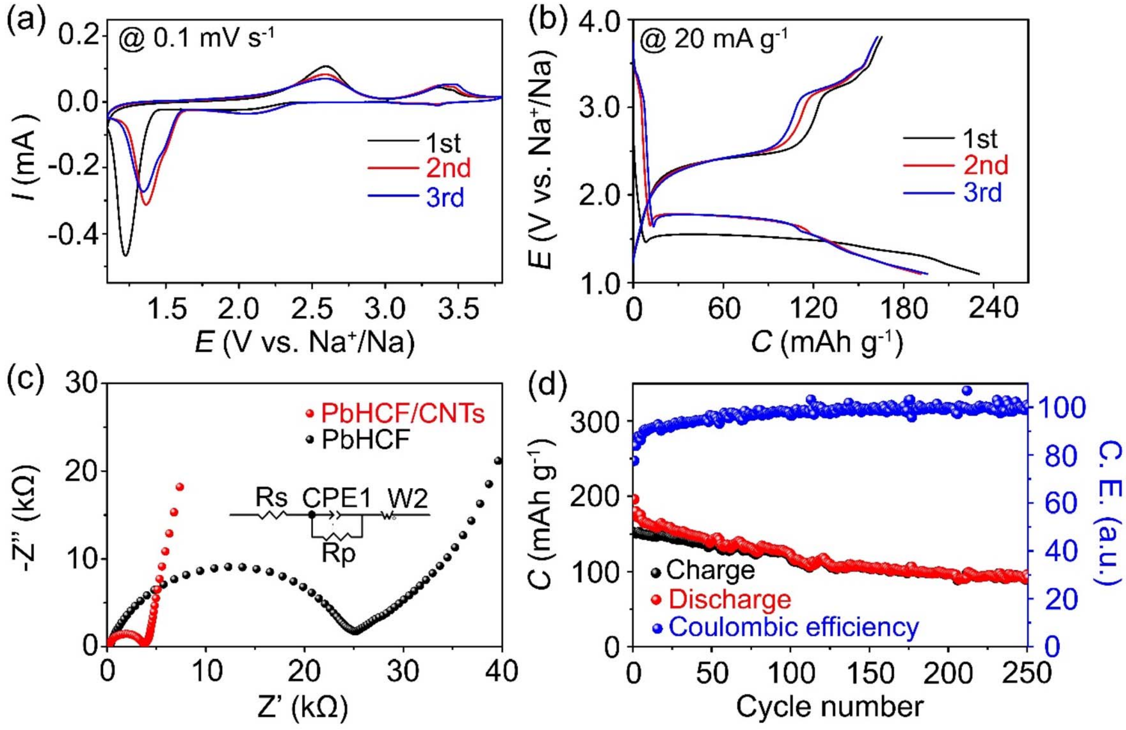

Fig. 3 (a) CV curves of PbHCF/CNTs at 0.1 mV s^{-1}; (b) charge/discharge curves of PbHCF/CNTs at 20 mA g^{-1}; (c) EIS curves of both PbHCF/CNTs and PbHCF; (d) cycling performance at 100 mA g^{-1} of PbHCF/CNTs in SIBs.

the synergistic effect induced by CNT incorporation. In the CV analysis (Fig. 3a), PbHCF/CNTs exhibits highly reversible redox behavior, as evidenced by the near-overlapping curves after the initial cycle. The slight deviation observed in the first cycle is attributed to electrolyte reduction and subsequent solid electrolyte interphase (SEI) layer formation. Two distinct cathodic peaks at 2.59 V and 3.46 V correspond to a two-step sodium storage mechanism involving the reduction of Pb^{2+} to Pb^0, accompanied by $Na_4Fe(CN)_6$ generation.[36] Conversely, the anodic scan reveals two oxidation peaks at 1.35 V and 3.36 V, confirming the reversible nature of these redox transitions. The GCD profiles of PbHCF/CNTs depicted in Fig. 3b exhibit two distinct discharge plateaus consistent with the CV results. The higher overpotential exhibited by the PbHCF/CNTs electrode in the initial cycle is likely due to the formation of SEI film and electrochemical activation. Notably, PbHCF/CNTs demonstrates enhanced cycling stability and lower polarization during the initial three cycles compared to PbHCF (Fig. S11†). The composite's exceptional rate capability is further demonstrated across current densities of 20–500 mA g^{-1} (Fig. S12†), delivering reversible capacities of 161.8, 142.7, 120.6, 95.4, and 54.3 mA h g^{-1} respectively. Remarkably, 97% of the initial capacity (156.3 mA h g^{-1}) is recovered when returning to 20 mA g^{-1}, indicating excellent structural stability. When compared to other PBA-based electrodes as shown in Table S3,† the PbHCF/CNTs cathode demonstrates superior electron transfer and a higher initial reversible capacity.

EIS analysis (Fig. 3c) reveals that PbHCF/CNTs possesses significantly lower charge-transfer resistance (144.7 Ω) than PbHCF (269.8 Ω), accounting for its enhanced rate performance. Long-term cycling tests at 100 mA g^{-1} (Fig. 3d) demonstrate a gradual capacity decline from 150.2 to 95.8 mA h g^{-1} over 250 cycles, corresponding to 64% capacity retention. GITT analysis (Fig. S13†) reveals stable Na^+ diffusion coefficients (10^{-10}–10^{-11} cm^2 s^{-1}) during (de)intercalation processes, suggesting efficient ion transport kinetics. This enhanced ionic mobility originates from the three-dimensional conductive network formed by CNTs interwoven with PbHCF particles. The interconnected architecture establishes electron-rich pathways that facilitate direct electron transfer to active sites while providing structural reinforcement, as supported by previous reports.[38,39] The Na^+ kinetic behavior of PbHCF/CNTs was also investigated using CV curves at different scanning rates (Fig. S14†). As the scanning rate increases, the shapes of the CV curves are almost the same. However, the cathode peak moves towards a higher value, while the anode peak moves negatively, which is caused by polarization. It indicates that the charge storage process of PbHCF/CNTs electrode is controlled by Faraday intercalation. While, as the scanning rate increases, the capacitive effect gradually takes the lead, indicating that PbHCF/CNTs can promote rapid charge transfer and enhance the diffusion ability of Na^+, thereby ensuring good rate performance for Na-storage.

The electrochemical reaction mechanism and structural evolution of PbHCF/CNTs electrodes were comprehensively elucidated through a multiscale characterization strategy integrating *operando* XRD, *in situ* FTIR, and *ex situ* XPS analyses. *Operando* XRD (Fig. 4a and b) captures the dynamic crystallographic phase transitions during the initial cycle. As the discharge proceeds, the diffraction peaks associated with PbHCF are gradually diminishing. At 1/4 of the discharge

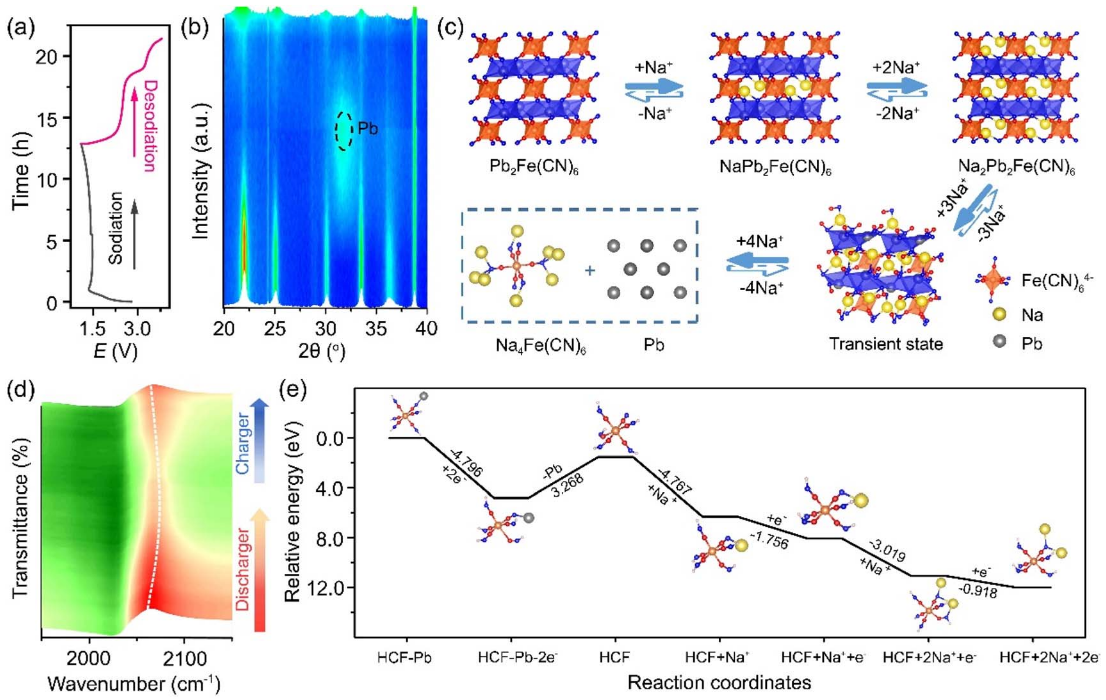

Fig. 4 (a) Charge/discharge curves of PbHCF/CNTs at 20 mA g^{-1}; (b) *operando* XRD results of PbHCF/CNTs during the first cycle; (c) schematic diagram of redox mechanism of PbHCF/CNTs cathode materials; (d) *in situ* FTIR contour map of PbHCF/CNTs during the first cycle; (e) schematic diagram of energy changes during discharging processes.

capacity (Dis. −1.4 V), the electrode retains the PbHCF structure, with a Na/Pb elemental ratio of approximately 1 : 2 (Fig. S15†). When discharged to 1.3 V (Dis. −1.3 V), a HRTEM image (Fig. S16a†) revealed a crystal plane with a spacing of 0.28 nm, likely corresponding to the (111) crystal plane of the Na_2PbHCF structure, which is a slightly smaller than that of the PbHCF, consisting with the XRD results in Fig. S17.† Upon discharging to 1.1 V (Dis. −1.1 V), the completely disappearance of characteristic PbHCF diffraction peaks (*e.g.*, 17.8° (200)) coincides with the emergence of a new broad Bragg reflection at 31.2° (JCPDS 04-0686), unequivocally confirming metallic Pb formation. However, there is no obvious lattice patterns were observed in the HRTEM image (Fig. S16b†), which can be attributed to the poor crystallinity of the discharge product. Notably, the full restoration of pristine XRD patterns at 3.8 V charging state demonstrates exceptional structural reversibility. As schematically illustrated in Fig. 4c, the Na-storage process proceeds *via* two sequential stages: (1) initial Na^+ insertion into PbHCF vacancies with minimal structural distortion *via* intercalation process, generating intermediate phases $NaPb_2Fe(CN)_6$ and $Na_2Pb_2Fe(CN)_6$; (2) subsequent conversion reaction yielding $Na_4Fe(CN)_6$ and Pb. The whole charge–discharge process involves a four-electron transfer electrochemical reaction, which has high reversibility and structural integrity. Furthermore, XRD peaks in Fig. S18† indicate minimal changes and good crystallinity of the PbHCF electrode after 100 cycles, demonstrating its structural stability. This indicates that the three-dimensional network structure of PbHCF/CNTs electrode material can effectively adapt to the volume changes and ensure robust structural integrity throughout the cycle.

To probe the ligand coordination dynamics, *in situ* FTIR (Fig. 4d) tracks the evolution of the Fe–C≡N–Pb stretching vibration at 2065 cm^{-1}. The gradual blueshift of this peak during discharging reflects the weakening of Pb^{2+} coordination, while its reversible restoration upon charging corroborates the redox reversibility. Complementarily, *ex situ* XPS (Fig. S19†) confirms the Pb^{2+}/Pb^0 redox couple participates in electron transfer, whereas Fe centers remain redox-inactive throughout cycling, aligning with the proposed mechanism. The sodium storage mechanism of $Pb_2Fe(CN)_6$ was further verified by *ex situ* XPS analysis. The valence state of Pb changes from Pb^{2+} to Pb^0 during discharge and returns to oxidation state during charging, which further verifies the four-electron transfer mechanism of $Pb_2Fe(CN)_6$.[42] It is worth noting that the valence state of Fe (Fig. S19b†) remains unchanged throughout the charge and discharge process. First-principles calculations further rationalize the energy landscape, as shown in Fig. 4e. PbHCF undergoes sequential two-electron reduction to form intermediate HCF, followed by Na^+ intercalation into the $Fe(CN)_6$ framework to stabilize Na_2HCF. The progressively decreasing binding energy along this pathway thermodynamically favors the four-electron reaction sequence.

In order to demonstrate the practical application of PbHCF, full cells were assembled with PbHCF/CNTs as the cathode and pre-sodiated hard carbon (HC) as the anode (HC‖PbHCF/CNTs, Fig. 5a). During discharge, Na^+ ions are released from the HC anode and migrate to the cathode, driving the sequential conversion of PbHCF to $Na_4Fe(CN)_6$ and metallic Pb *via* the established four-electron mechanism. Reverse ion transport during charging regenerates the original phases, confirming the

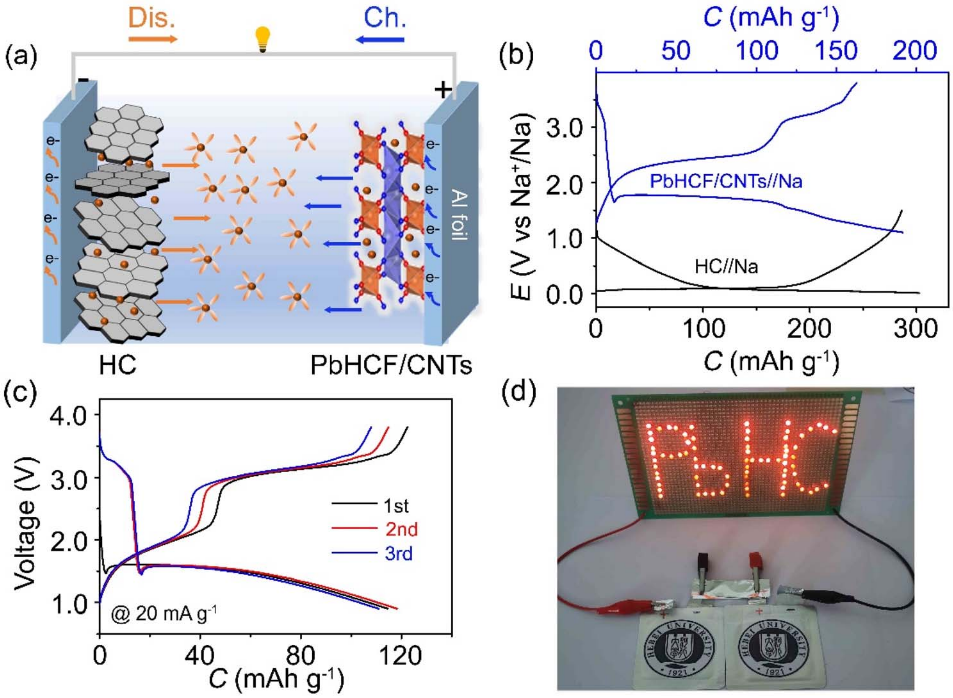

Fig. 5 (a) Schematic diagram of HC‖PbHCF/CNTs full cell; (b) charge/discharge curves of Na‖HC and Na‖PbHCF/CNTs half cells; (c) charge/discharge curves of HC‖PbHCF/CNTs full cell for the first three cycles at 20 mA g^{-1}; (d) soft pack batteries light up "PbHC" LEDs.

system's intrinsic reversibility. The complementary charge/discharge profiles of individual HC and PbHCF/CNTs half-cells (Fig. 5b) exhibit compatible operating potentials (0.01–1.0 V *vs.* Na^+/Na for HC; 1.5–3.8 V *vs.* Na^+/Na for PbHCF/CNTs), ensuring effective full-cell operation within 0.9–3.8 V. At 20 mA g^{-1}, the full cell delivers initial discharge/charge capacities of 122.3/114.5 mA h g^{-1} (Fig. 5c), corresponding to an initial coulombic efficiency of 93.6%. The near-overlap of voltage profiles across three consecutive cycles underscores exceptional reaction reversibility. The energy density of this system based on the PbHCF/CNTs cathode and HC anode active material is calculated to be approximately 117.5 Wh kg^{-1} (based on the active materials of the anode and cathode), surpassing the values of most reported PBA-based full cells.[8,16] Long cycling (Fig. S20†) reveals capacity stabilization at 78.7 mA h g^{-1} after 50 cycles with coulombic efficiency approaching 100%, indicative of stable interfacial kinetics. Notably, a laboratory-scale HC||PbHCF/CNTs pouch cell (Fig. 5d) successfully illuminated an LED display labeled “PbHC”, providing tangible evidence of the system's energy delivery capability. This practical demonstration, combined with the benign cost structure of PBAs, positions PbHCF/CNTs as a viable cathode candidate for scalable SIB technologies.

Conclusions

In conclusion, a new cathode material (PbHCF/CNTs) with significant potential for SIBs was synthesized using a straightforward co-precipitation method. The unique architecture synergistically integrates multi-electron redox chemistry with nanoscale conductive networks, where the Pb^{2+}/Pb^0 redox couple enable a four-electron transfer mechanism while the CNT matrix ensures rapid charge transport and strain accommodation. This configuration delivers exceptional electrochemical performance, including a record-high initial capacity of 161.8 mA h g^{-1} (20 mA g^{-1}) among Prussian blue analogues (PBAs), a good rate capability (54.3 mA h g^{-1} at 500 mA g^{-1}), and 64% capacity retention after 250 cycles. *Operando* XRD and *in situ* FTIR analyses confirm the structural reversibility through continuous PbHCF ↔ $Na_4Fe(CN)_6$ phase transitions and stable ligand coordination during cycling. Practical viability is further evidenced by full-cell configurations (HC||PbHCF/CNTs) achieving 114.5 mA h g^{-1} cathode capacity and successful powering LED demonstrations. Our findings establish a new paradigm for PBA-based cathodes, highlighting the critical roles of multi-electron transfer reactions and conductive nanostructure in overcoming the capacity–stability trade-off.

Data availability

The data supporting this article have been included as part of the ESI.†

Author contributions

Na Liu: investigation, validation, data curation, formal analysis. Xiaohan Wang: software, methodology, formal analysis. Jing Liu: methodology, formal analysis. Ningbo Liu: formal analysis. Liubin Wang: conceptualization, supervision, software, writing – review & editing, project administration.

Conflicts of interest

There are no conflicts to declare.

Acknowledgements

Financial supports from the National Natural Science Foundation of China (22109037), Youth Talent Project of Hebei Provincial Department of Education (BJ2025113), Multidisciplinary Research Project of Hebei University (DXK202309), and Hebei Province Innovation Capability Enhancement Plan Project (22567620H) are acknowledged.

Notes and references

1 Y. Zhao, Y. Kang, J. Wozny, J. Lu, H. Du, C. Li, T. Li, F. Kang, N. Tavajohi and B. Li, Recycling of sodium-ion batteries, *Nat. Rev. Mater.*, 2023, **8**(9), 623–634.

2 Z. Zhu, T. Jiang, M. Ali, Y. Meng, Y. Jin, Y. Cui and W. Chen, Rechargeable batteries for grid scale energy storage, *Chem. Rev.*, 2022, **122**(22), 16610–16751.

3 D. Larcher and J.-M. Tarascon, Towards greener and more sustainable batteries for electrical energy storage, *Nat. Chem.*, 2015, **7**(1), 19–29.

4 J. Wang, Y.-F. Zhu, Y. Su, J.-X. Guo, S. Chen, H.-K. Liu, S.-X. Dou, S.-L. Chou and Y. Xiao, Routes to high-performance layered oxide cathodes for sodium-ion batteries, *Chem. Soc. Rev.*, 2024, **53**(8), 4230–4301.

5 F. Wang, Z. Jiang, Y. Zhang, Y. Zheng, J. Li, H. Wang, T. Jiang, G. Xing, H. Liu and Y. Tang, Revitalizing sodium-ion batteries via controllable microstructures and advanced electrolytes for hard carbon, *eScience*, 2023, **4**(3), 100181.

6 X. Liang, J.-Y. Hwang and Y. K. Sun, Practical cathodes for sodium-ion batteries: who will take the crown?, *Adv. Energy Mater.*, 2023, **13**(37), 2301975.

7 N. Liu, X. Zhao, B. Qin, D. Zhao, H. Dong, M. Qiu and L. Wang, A high-performance Na-storage cathode enabled by layered P2-type $KxMnO_2$ with enlarged interlayer spacing and fast diffusion channels for sodium-ion batteries, *J. Mater. Chem. A*, 2022, **47**(10), 25168–25177.

8 Z. Jing, M. Mamoor, L. Kong, *et al.*, Rational design of cobalt-based Prussian blue analogues via 3d transition metals incorporation for superior Na-ion storage, *Angew. Chem., Int. Ed.*, 2025, **64**(15), e202423356.

9 S. Liu, L. Wang, J. Liu, M. Zhou, Q. Nian, Y. Feng, Z. Tao and L. Shao, $Na_3V_2(PO_4)_2F_3$-SWCNT: a high voltage cathode for non-aqueous and aqueous sodium-ion batteries, *J. Mater. Chem. A*, 2019, **7**(1), 248–256.

10 Y. Xiao, J. Xiao, H. Zhao, *et al.*, Prussian blue analogues for sodium-ion battery cathodes: a review of mechanistic insights, current challenges, and future pathways, *Small*, 2024, **20**(35), 2401957.

11 T. Chen, J. Wang, B. Tan, K. Zhang, H. Banda, Y. Zhang, D.-H. Kim and M. Dincă, High-energy, high-power sodium-

ion batteries from a layered organic cathode, *J. Am. Chem. Soc.*, 2025, **147**(7), 6181–6192.

12 H. Wang, H. Chen, Y. Mei, *et al.*, Manipulating local chemistry and coherent structures for high-rate and long-life sodium-ion battery cathodes, *ACS Nano*, 2024, **18**(20), 13150–13163.

13 L. Wang, N. Liu, X. Zhao, X. Wang, T. Zhang, Z. Luo and F. Li, Copper and conjugated carbonyls of metal-organic polymers as dual redox centers for Na storage, *Chem. Sci.*, 2024, **15**(6), 2133–2140.

14 J. Liang, P. Xiao, J. Cheng, M. Gong, W. Teng, J. Liu, H. Liu and D. Wang, Enhancing the structure stability and sodium storage performance of P2-$Na_{2/3}Ni_{1/3}Mn_{2/3}O_2$ via Ti-doped, *Energy Lab.*, 2024, **2**(2), 240001.

15 P. Hong, C. Xu, C. Yan, Y. Dong, H. Zhao and Y. Lei, Prussian blue and its analogues for commercializing fast-charging sodium/potassium-ion batteries, *ACS Energy Lett.*, 2025, **10**(2), 750–778.

16 X. Zhao, N. Liu, M. Zheng, X. Wang, Y. Xu, J. Liu, F. Li and L. Wang, Four-electron redox reaction in Prussian blue analogues cathode material for high-performance sodium-ion batteries, *ACS Energy Lett.*, 2024, **9**(6), 2748–2757.

17 X.-Y. Fu, L.-L. Zhang, C.-C. Wang, H.-B. Sun and X.-L. Yang, Recent progress of Prussian blue analogues as cathode materials for metal ion secondary batteries, *Rare Met.*, 2025, **44**(1), 34–59.

18 Y. Xiao, J. Xiao, H. Zhao, *et al.*, Prussian blue analogues for sodium-ion battery cathodes: a review of mechanistic insights, current challenges, and future pathways, *Small*, 2024, **20**(35), 2401957.

19 K. Wang, M. Yang, Q. Liu, S. Cao, Y. Wang, T. Hu and Z. Peng, Acid-assisted synthesis of core-shell Prussian blue cathode for sodium-ion batteries, *J. Colloid Interface Sci.*, 2025, **678**, 346–358.

20 L. Li, J. Shen, H. Yang, Z. Li, Z. Chen, Y. Yao, W. Li, X. Wu, X. Rui and Y. Yu, Selection rules of transition metal dopants for Prussian blue analogs enabling highly reversible sodium storage, *Adv. Energy Mater.*, 2024, **14**(29), 2401729.

21 J. Cattermull, M. Pasta and A. L. Goodwin, Structural complexity in Prussian blue analogues, *Mater. Horiz.*, 2021, **8**(12), 3178–3186.

22 X. Lou, Z. Li, S. Kang, Y. Li, S. Ma, F. Geng and B. Hu, In situ electron paramagnetic resonance reveals fading mechanism of Mn-based Prussian blue analogue: accelerated Mn dissolution due to charge delocalization, *Renewables*, 2024, **2**(5), 341–352.

23 R. Wilde, S. Ghosh and B. Marshall, Prussian blues, *Inorg. Chem.*, 1970, **9**(11), 2512–2516.

24 J. Qian, C. Wu, Y. Cao, Z. Ma, Y. Huang, X. Ai and H. Yang, Prussian blue cathode materials for sodium-ion batteries and other ion batteries, *Adv. Energy Mater.*, 2018, **8**(17), 1702619.

25 L. Wang, J. Song, R. Qiao, *et al.*, Rhombohedral Prussian white as cathode for rechargeable sodium-ion batteries, *J. Am. Chem. Soc.*, 2015, **137**(7), 2548–2554.

26 Y. Xu, J. Wan, L. Huang, *et al.*, Dual redox-active copper hexacyanoferrate nanosheets as cathode materials for advanced sodium-ion batteries, *Energy Storage Mater.*, 2020, **33**, 432–441.

27 X. Wu, C. Wu, C. Wei, L. Hu, J. Qian, Y. Cao, X. Ai, J. Wang and H. Yang, Highly crystallized $Na_2CoFe(CN)_6$ with suppressed lattice defects as superior cathode material for sodium-ion batteries, *ACS Appl. Mater. Interfaces*, 2016, **8**(8), 5393–5399.

28 Y. Xu, M. Ou, Y. Liu, J. Xu, X. Sun, C. Fang, Q. Li, J. Han and Y. Huang, Crystallization-induced ultrafast Na-ion diffusion in nickel hexacyanoferrate for high-performance sodium-ion batteries, *Nano Energy*, 2020, **67**, 104250.

29 L. Wang, Y. Lu, J. Liu, M. Xu, J. Cheng, D. Zhang and J. Goodenough, A superior low-cost cathode for a Na-ion battery, *Angew. Chem., Int. Ed.*, 2013, **52**(7), 1964–1967.

30 H. Yi, R. Qin, S. Ding, Y. Wang, S. Li, Q. Zhao and F. Pan, Structure and properties of Prussian blue analogues in energy storage and conversion applications, *Adv. Funct. Mater.*, 2021, **31**(6), 2006970.

31 Y. Yang, E. Liu, X. Yan, C. Ma, W. Wen, X. Liao and Z. Ma, Influence of structural imperfection on electrochemical behavior of Prussian blue cathode materials for sodium ion batteries, *J. Electrochem. Soc.*, 2016, **163**(9), A2117–A2123.

32 B. Xie, B. Sun, T. Gao, Y. Ma, G. Yin and P. Zuo, Recent progress of Prussian blue analogues as cathode materials for nonaqueous sodium-ion batteries, *Coord. Chem. Rev.*, 2022, **460**, 214478.

33 L. Wang, N. Liu, Q. Li, X. Wang, J. Liu, Y. Xu, Z. Luo, N. Zhang and F. Li, Dual redox reactions of silver hexacyanoferrate Prussian blue analogue enable superior electrochemical performance for zinc-ion storage, *Angew. Chem., Int. Ed.*, 2025, **64**(4), e202416392.

34 T. Yuan, Y. Chen, X. Gao, R. Xu, Z. Zhang, X. Chen and L. Cui, Research progress of Prussian blue and its analogs as high-performance cathode nanomaterials for sodium-ion batteries, *Small Methods*, 2024, **8**(8), 2301372.

35 Y. You, H. You, Y. Yin, T. Zuo, C. Yang, Y. Guo, Y. Cui, L. Wang and J. Goodenough, Subzero-temperature cathode for a sodium-ion battery, *Adv. Mater.*, 2016, **28**(33), 7243–7248.

36 W. Tang, Y. Xie, F. Peng, *et al.*, Electrochemical performance of $NaFeFe(CN)_6$ prepared by solid reaction for sodium ion batteries, *J. Electrochem. Soc.*, 2018, **165**(16), A3910–A3917.

37 V. G. Zubkov, A. P. Tyutyunnik, I. F. Berger, L. G. Maksimova, T. A. Denisova, E. V. Polyakov, I. G. Kaplan and V. I. Voronin, Anhydrous tin and lead hexacyanoferrates (II): Part I. synthesis and crystal structure, *Solid State Sci.*, 2001, **3**(3), 361–367.

38 J. Guo, Y. Wang, Y. Cai, H. Zhang, Y. Li and D. Liu, Ni-doping Cu-Prussian blue analogue/carbon nanotubes composite (Ni-CuPBA/CNTs) with 3D electronic channel-rich network structure for capacitive deionization, *Desalination*, 2022, **528**, 115622.

39 D. Zhao, N. Zhang, X. Zhao, N. Liu, B. Qin, M. Qiu and L. Wang, A novel PbSe@CNTs anode material based on

dual conversion-alloying mechanism for sodium-ion batteries, *Sci. China Mater.*, 2023, **66**(1), 61–68.

40 S. Kettle, E. Diana, E. Marchese, E. Boccaleri and P. Stanghellini, The vibrational spectra of the cyanide ligand revisited: the ν(CN) infrared and Raman spectroscopy of Prussian blue and its analogues, *J. Raman Spectrosc.*, 2011, **42**(11), 2006–2014.

41 Z. Jin, H. Gao and L. Hu, Removal of Pb(II) by nano-titanium oxide investigated by batch, XPS and model techniques, *RSC Adv.*, 2015, **107**(5), 88520–88528.

42 X. Wang, N. Liu, M. Zhang, X. Zhao, J. Liu and L. Wang, Valence switching of bismuth in ferricyanide as cathode materials for sodium-ion batteries, *J. Power Sources*, 2025, **625**, 235666.